

Ab Initio Molecular Dynamics Study of Crystalline Nitric Acid Trihydrate

Doris M. Sullivan,[†] Ken Bagchi,[†] Mark E. Tuckerman,[‡] and Michael L. Klein^{*,†}

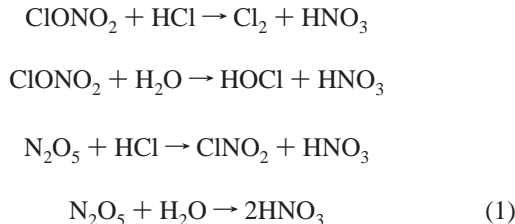
Center for Molecular Modeling and Department of Chemistry, University of Pennsylvania, Philadelphia, Pennsylvania 19104-6323, and Department of Chemistry, New York University, New York, New York 10003

Received: March 26, 1999; In Final Form: July 19, 1999

Ab initio based Car-Parrinello molecular dynamics calculations (CPMD) have been used to investigate the properties of crystalline nitric acid trihydrate (NAT) at 195 K. The crystal unit cell consists of four formula units of NAT and nominally contains the ions NO_3^- and H_3O^+ plus H_2O molecules. Reversible proton-transfer events were observed between unique H_3O^+ and neighboring H_2O pairs, which occur throughout the crystal. Full proton transfer to form a new neighboring H_3O^+ molecule was a rare event. The motion of this mobile proton was associated with hyperextension of the covalent oxygen–hydrogen of H_3O^+ , whose stretch frequency was observed in corresponding power spectra. Calculations showed that a classical free energy of $3.3 k_B T$ was required for the proton to reach the center of the oxygen–oxygen pair. Crystalline NAT was further characterized by calculated equilibrium averages, structural properties, and vibrational spectra.

I. Introduction

Antarctic polar stratospheric clouds (PSCs) are classified into Types I and II, where Type I PSCs are thought to be mainly composed of nitric acid trihydrate (NAT) crystals.^{1,2} It has been hypothesized that Type I PSCs play a crucial role in the chemical processes responsible for the ever-expanding ozone hole over Antarctica.³ For example, the heterogeneous reactions



that take place slowly in the gas phase occur rapidly on model PSC surface films.^{4,5} Thus, normally stable chlorine reservoirs of ClONO_2 and HCl are readily converted to highly reactive chlorine products of HOCl , Cl_2 , and ClNO_2 . Subsequent conversion via sunlight photolysis to free chlorine catalyzes the destruction of ozone. Furthermore, HNO_3 products from the heterogeneous reactions are permanently removed by sedimentation, resulting in lower levels of available NO_x (i.e., denitrification) that can convert unstable ClO back to stable ClONO_2 .

Thus noting the importance of PSCs in the ozone destruction process, the present work investigates the crystalline properties of NAT, prevalent in Type I PSCs,² using ab initio computer simulation methods. The published crystal structure,⁶ containing both hydronium H_3O^+ and nitrate NO_3^- ions, shows H_3O^+ closely hydrogen bonded to two adjacent water sites. Since proton transfer is thought to occur between H_3O^+ and H_2O , to form the intermediate H_5O_2^+ complex,^{6,7} ab initio MD methods are used to give a good model of the bond-breaking and formation in the NAT crystal. Recent ab initio studies of the

monohydrate form of the crystal (NAM),⁸ also present in Type I PSCs, have shown reversible proton transfer between H_3O^+ and NO_3^- . However, to date, the trihydrate form has not been investigated by theoretical techniques.

Ab initio Car–Parrinello (CP) molecular dynamics (MD)⁹ was used to simulate the NAT crystal at the atmospherically relevant temperature of 195 K. Rather than relying on empirical potential functions, CPMD obtains internuclear forces from an “on the fly” density functional theory (DFT) based electronic structure calculation. CP calculations of the geometries of nitric acid and water clusters ($\text{NO}_3(\text{H}_2\text{O})_n$, $n = 1, 2, 3$) in the gas phase have shown good agreement with high level electronic structure calculations.¹⁰ We present equilibrium properties and distribution functions for the crystal and compare the existing experimental vibrational spectra^{11–16} to our power spectra calculated from the CPMD trajectory.

2. Methods

A. Ab Initio CPMD. The CP methodology employs a density functional theory (DFT) description of electronic structure and is based on the Hohenberg–Kohn variational principle.⁷ This states that the ground-state electronic energy E_0

$$E_0 = \min_{\{\phi_i\}} E[\{\phi_i\}, \{\mathbf{R}_I\}] \quad (2)$$

is the minimum of the Kohn–Sham (KS) energy functional $E[\{\phi_i\}, \{\mathbf{R}_I\}]$, which is a function of KS orbitals $\{\phi_i\}$ and nuclear $\{\mathbf{R}_I\}$ degrees of freedom and has the form¹⁸

$$\begin{aligned} E[\{\phi_i\}, \{\mathbf{R}_I\}] = & -\frac{1}{2} \sum_i \langle \phi_i | \nabla^2 | \phi_i \rangle + \\ & \frac{1}{2} \iint d\mathbf{r} d\mathbf{r}' \frac{n(\mathbf{r})n(\mathbf{r}')}{|\mathbf{r} - \mathbf{r}'|} + E_{xc}[n] + \int d\mathbf{r} n(\mathbf{r}) V_{loc}(\mathbf{r}, \{\mathbf{R}_I\}) + \\ & \sum_i \langle \phi_i | \hat{V}_{NL}(\{\mathbf{R}_I\}) | \phi_i \rangle + \sum_{I < J} \frac{Z_I Z_J}{|\mathbf{R}_I - \mathbf{R}_J|} \end{aligned} \quad (3)$$

[†] Center for Molecular Modeling and Department of Chemistry.

[‡] Department of Chemistry.

where atomic units have been employed. The minimization is carried out subject to an orthonormality constraint where $\langle \phi_i | \phi_j \rangle = \delta_{ij}$. The above equation gives the electron density $n(\mathbf{r}) = \sum_i |\phi_i(\mathbf{r})|^2$ as a sum over occupied states i . It also includes terms for the kinetic and Hartree energies, electron exchange and correlation functional E_{xc} , local V_{loc} and nonlocal V_{NL} pseudopotential contributions, and ion-ion Coulombic energies, respectively. The required basis set is reduced in size by the use of atomic pseudopotentials, which eliminate the core electrons. Thus the KS orbitals $\{\phi_i\}$ give the electronic structure of the valence electrons in the field of classical ions $\{\mathbf{R}_I\}$, which consist of both nuclei and attached core electrons.

Rather than relying on a traditional self-consistent method to solve the KS equations $H_{KS}|\phi_i\rangle = \epsilon_i|\phi_i\rangle$, the ground-state density n_0 and KS orbitals $\{\phi_i\}$ can be obtained by using the Car-Parrinello (CP) molecular dynamics method.⁹ In CPMD, an extended Lagrangian is formulated as

$$\mathcal{L} = \mu \sum_i \langle \dot{\phi}_i | \dot{\phi}_i \rangle + \frac{1}{2} \sum_I M_I \dot{\mathbf{R}}_I^2 - E[\{\phi_i\}, \{\mathbf{R}_I\}] + \sum_{ij} \Lambda_{ij} (\langle \phi_i | \phi_j \rangle - \delta_{ij}) \quad (4)$$

The first term in eq 4 corresponds to a fictitious kinetic energy with fictitious mass parameter μ (having units of energy·time²), and M_I is the classical ionic mass of ion I . The final term in eq 4, which involves a set of Lagrange multipliers Λ_{ij} , is used to impose the orthonormality condition on the orbitals.^{19–22}

MD equations of motion for the classical ions $\{\mathbf{R}_I\}$ and KS orbitals $\{\phi_i\}$ are derived from the Lagrangian in eq 4.²² The ions $\{\mathbf{R}_I\}$ evolve from both Coulomb ion-ion forces and Hellmann-Feynman force contributions from the KS energy functional. The KS orbitals $\{\phi_i\}$ execute a fictitious adiabatic “dynamics” that allows them to follow the nuclear motion and fluctuate with small amplitude about the exact ground-state surface. The electronic adiabaticity is maintained through the use of Nosé-Hoover chain thermostats,²³ in a “knotted” chain scheme,^{22,24} and through the choice of μ , whereby the fictitious kinetic energy is kept small compared to that of the nuclei while allowing the electrons to move rapidly in response to nuclear displacements.^{22,25,26}

B. Computational Details. The initial coordinates for the NAT crystal were taken from the published crystal structure obtained at $T = 85$ K. The orthorhombic NAT crystal unit cell has four HNO_3 (H_2O)₃ units, containing the ions NO_3^- and H_3O^+ , and belongs to the space group $P2_12_12_1$. Three unit cells of NAT (168 atoms total) were placed in a simulation box ($10.564 \text{ \AA} \times 14.687 \text{ \AA} \times 9.485 \text{ \AA}$). Because the crystal was studied at a finite temperature of 195 K, a 2.5% volume expansion was allowed for primarily in the direction of the crystallographic c axis. The chosen volume expansion was thought to be reasonable based upon X-ray studies of crystalline heavy ice,²⁷ where a 1.3% uniform thermal volume expansion occurred from $T = 123\text{--}223$ K.

All calculations were performed using the CPMD ab initio molecular dynamics package.²⁸ Electron exchange and correlation were treated at the generalized gradient approximation (GGA) level²⁹ using the Becke (B) exchange³⁰ and Lee, Yang, and Parr (LYP) correlation functionals.³¹ The BLYP scheme has been shown to give a reasonably good description of aqueous hydrogen bonding and excellent results for intermolecular O–O distances.³² Moreover, structural findings for small charged water clusters in the gas phase compare well³³ to high level fully correlated quantum electronic structure calculations.³⁴

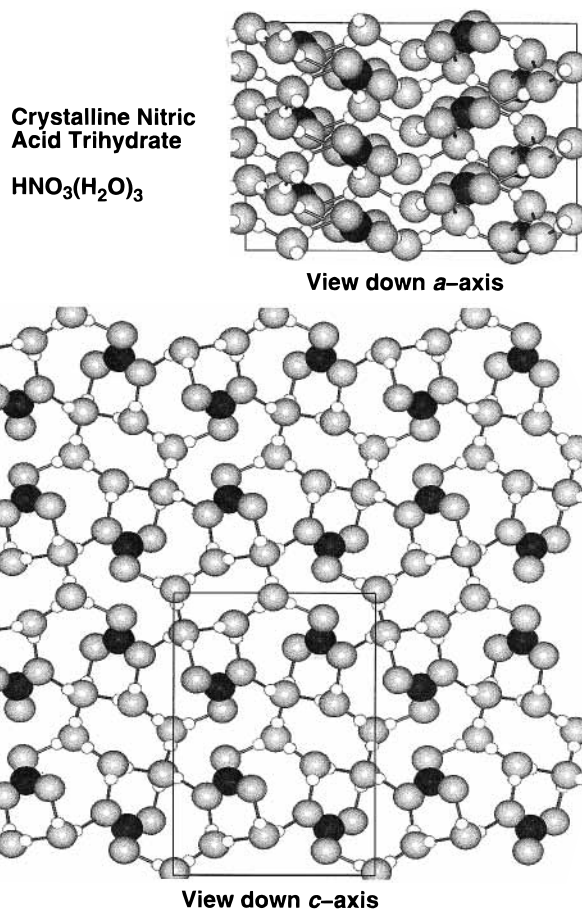


Figure 1. Views down the crystallographic a and c axes of crystalline NAT. The simulation cell, containing 3 unit cells, is shown within the box outline. Hydrogen, oxygen, and nitrogen are shown using their covalent radii in white, gray, and black, respectively. Hydrogen bonds in the crystal are drawn with gray lines.

Atomic pseudopotentials of the Troullier and Martins form³⁵ were used to take into account the effect of the core electrons, and a 70 Rydberg energy cutoff was used in the plane wave expansion of the KS orbitals.

An initial geometry minimization was performed for about 100 steps to relax the bond lengths. Afterward, an equilibration period of 3 ps with the ions and electrons thermostated at 195K using Nosé-Hoover chains^{33,36} of length 4. The fictitious electron mass was assigned to be 600 au, and a time step of 0.12 fs was chosen. At this point, the ionic thermostats were removed and a final trajectory of 5 ps was obtained.

3. Results and Discussion

The initial MD configuration (after geometry minimization) of perfect crystalline NAT is shown in Figure 1 with views down the crystallographic a and c axes, where H_3O^+ is hydrogen bonded to the oxygens of two waters and NO_3^- . There are seven unique hydrogen bonds (shown as q_n coordinates), forming a pattern that occurs four times within the unit cell and twelve times overall within the simulation cell (see Figures 1 and 2). The hydrogen bonding network is shown in detail in Figure 2 where the asymmetric stretch coordinates

$$q_n = |\mathbf{R}_{\text{O}_x\text{H}_n}| - |\mathbf{R}_{\text{O}_y\text{H}_n}| \quad (5)$$

are defined from $n = 1\text{--}7$ and $\mathbf{R}_{\text{O}_x\text{H}_n}$ denotes the $\text{O}_x\text{--H}_n$ vector for a given oxygen x and proton n . The H_3O^+ is significantly

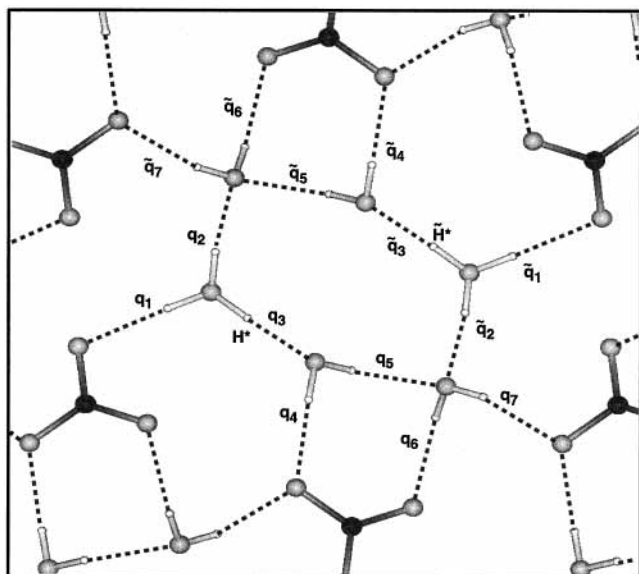


Figure 2. The hydrogen bonding network of crystalline NAT with unique asymmetric stretch coordinates (q_1 – q_7) labeled. Repeat units are given as (\tilde{q}_1 – \tilde{q}_7). H^* denotes the mobile proton (see Figure 3). Hydrogen, oxygen, and nitrogen are shown as white, gray, and black, respectively, and hydrogen bonds are drawn as dotted lines.

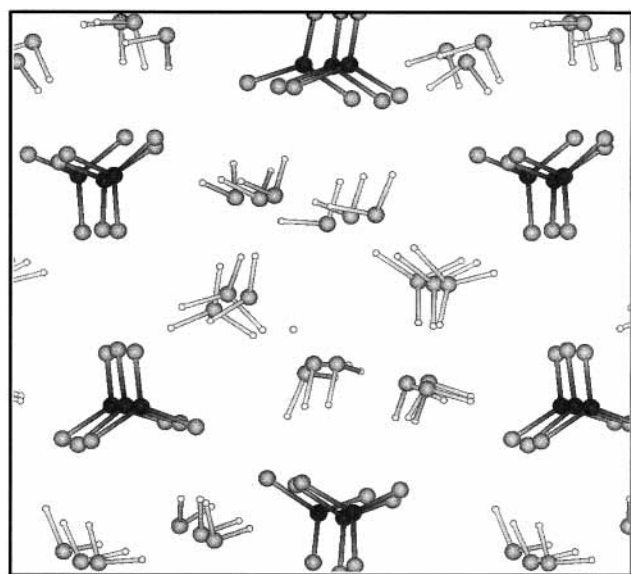


Figure 3. Instantaneous configuration of crystalline NAT at 195 K from a CPMD trajectory. The mobile proton H^* is seen in the center of the two neighboring water molecules. Hydrogen, oxygen, and nitrogen are shown as white, gray, and black, respectively.

closer to the nearest water defined by the q_3 coordinate and the O–O distance (R_{OO}^3) is ~ 2.5 Å in the initial crystal structure. Thus, on the basis of R_{OO}^3 distance and anticipating our simulation results, the mobile proton $H^* \equiv H_3$ is labeled in Figure 2 for reference.

As expected from the R_{OO}^3 lengths within the initial crystal structure, the proton was observed to transfer toward the middle of the q_3 coordinate and toward the nearest water during the simulation. An instantaneous snapshot from the CPMD trajectory at 195 K is shown in Figure 3, where within a q_3 coordinate, an H^* has dissociated from H_3O^+ to form a short-lived $H_5O_2^+$ species. Full proton transfer to form a stable, neighboring H_3O^+ rarely occurred. Rather, H^* preferred to reform its original H_3O^+ covalent bond and most H^* motion involved a noticeable elongated stretching of its covalent bond.

TABLE 1: Average CP Bond Distances \pm Root Mean Square Errors (σ) for Crystalline NAT at 195 K^a

bond	distance $\pm \sigma$ / Å
N–O (NO_3^-)	1.27, 1.28, 1.29 \pm 0.02
O–H (H_2O)	1.00 \pm 0.02
O–H ₁ (H_3O^+)	1.04 \pm 0.03
O–H ₂ (H_3O^+)	1.00 \pm 0.02
O–H* (H_3O^+)	1.09 \pm 0.05

^a O–H_n corresponds to the covalent bond contained within the q_n coordinate. The mobile proton $H^* \equiv H_3$.

TABLE 2: Average CP Intermolecular Oxygen–Oxygen (OO) Nearest-Neighbor (NN) Distances \pm Root Mean Square Errors (σ) and Distribution Widths (2σ) for Crystalline NAT at 195 K^a

OO pair	distance $\pm \sigma$ / Å	2σ / Å
R^1	2.65 \pm 0.09	0.17
R^2	2.59 \pm 0.07	0.13
R^3	2.51 \pm 0.06	0.12
R^4	2.85 \pm 0.11	0.21
R^5	2.78 \pm 0.09	0.18
R^6	2.79 \pm 0.10	0.21
R^7	2.75 \pm 0.09	0.19

^a R^n is the NN OO pair distance defined by the corresponding q_n coordinate. The mobile proton H^* is located between the R^3 NN OO pair.

A. Average and Structural Properties. The average distances were calculated for the bond lengths within the NO_3^- , H_2O , and H_3O^+ molecules and presented in Table 1. Calculated N–O bond lengths of 1.27, 1.28, 1.29 \pm 0.02 Å are within error estimates for bond lengths of 1.25, 1.26, 1.27 Å obtained from X-ray measurements.⁶ Even at 85 K, the experimental isotropic thermal parameter B is significantly larger for a particular hydrogen (labeled H(5) in ref 6) and as expected, H(5) corresponds to H^* in our calculations.

The O–H bond lengths from H_2O were found to be equivalent with bond lengths of 1.00 \pm 0.02 Å, while the O–H bonds from H_3O^+ were found to have differing bond lengths. In particular, the O– H^* bond of H_3O^+ was elongated significantly to 1.09 \pm 0.05 Å. The shorter 1.04 \pm 0.03 Å O–H₁ and 1.00 \pm 0.02 Å O–H₂ bonds were hydrogen bonded to the NO_3^- and H_2O groups, respectively.

The average nearest-neighbor (NN) intermolecular oxygen–oxygen (OO) pair distances R_{OO}^3 were also calculated (see Table 2) and labeled to specify oxygen pairs contained within the q_n coordinates in Figure 2. The distribution functions for each pair are Gaussian shaped and thus their widths of 2σ are reported as well. The length $R_{OO}^3 \equiv R_{OO}^*$ has a value of $R = 2.51 \pm 0.06$ Å and width of $2\sigma = 0.12$ Å. The remaining O–O distances are on average greater than 2.5 Å, which is consistent with the lack of proton transfer observed between those O–O pairs. Distribution widths were found to increase with increasing average distances during the 5 ps of simulation time.

In Figure 4, the crystalline structure is shown in the calculated radial pair distribution functions $g(r_{XX})$ for the $XX = NN, OO,$ and OH distances. For reference, the $g(r)$ s of the “perfect” crystal structure are also included. The crystalline structure is easily seen in the distinct peak structure of $g(r_{NN})$ in Figure 4a. In comparison to the “perfect” crystal, results from the CPMD simulation at 195 K indicate a splitting of the first $g(r_{NN})$ peak. Although the peak splitting is fairly large, calculated correlation functions from pair distances and velocities display ringing and lack of decorrelation in all x –, y –, and z – components, indicating that the crystal is stable. However, the experimental structure at 85 K⁶ gave rms anisotropic thermal parameters (U_{ij})

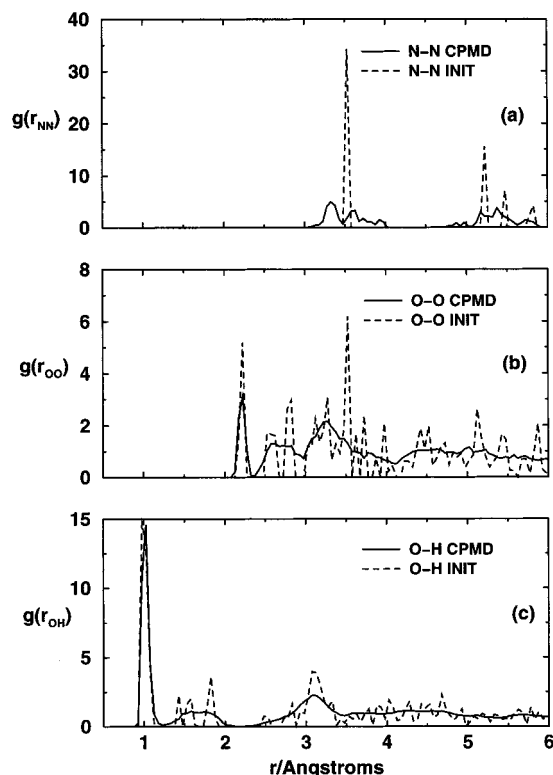


Figure 4. Radial distribution functions for crystalline NAT at 195 K calculated from a CPMD trajectory (solid lines) and the initial configuration of the perfect crystal (dashed lines). The distributions are shown for the (a) nitrogen–nitrogen (NN), (b) oxygen–oxygen (OO), and (c) oxygen–hydrogen (OH) pair distances.

along the principal axes of the vibrational ellipsoids that were not significantly greater for nitrogen in comparison to oxygen. Therefore, although the peak splittings found in $g(r_{NN})$ could be attributed to the increased temperature $T = 195$ K of the simulation, they may be, in part, an artifact due to the initial nonuniform expansion of the simulation cell.

The $g(r_{OO})$ distribution function is shown in Figure 4b where the thermal motions in the crystal have filled in the gaps between discrete peaks that occur for the perfect crystal. The first peak (~ 2.2 Å) corresponds to the intramolecular OO distances within the NO_3^- group followed by the peaks for the intermolecular NN–OO distances whose individual average values are tabulated in Table 2. The OH distribution function is shown in Figure 4c where the first peak is attributed to the O–H covalent bonds. The effect of H^* motions are shown as a slight broadening in the wings of the first peak.

The q_n coordinates are defined in eq 5 and shown for crystalline NAT in Figure 2. For our system, the first oxygen O_a is defined to be the oxygen that H_n is originally bound by (see eq 5). During proton transfer, the q_n coordinate will always start out negative and increase toward zero as the proton reaches the center of the OO pair. q changes to positive values and increases as the proton forms a new bond with the neighboring oxygen. With the exception of $P(q_3)$, the calculated $P(q_n)$ distribution functions showed well defined density only in negative q regions, indicating that these covalent bonds remained intact during the simulation. In Figure 5a, $P(q_3)$, containing H^* , showed density in both positive and negative regions. However, the $P(q_3)$ density was low in positive regions, indicating that full proton transfer occurred rarely and most of the H^* motion involved the hyperextension of the O– H^* covalent bond associated with H_3O^+ . The localization of proton motion within

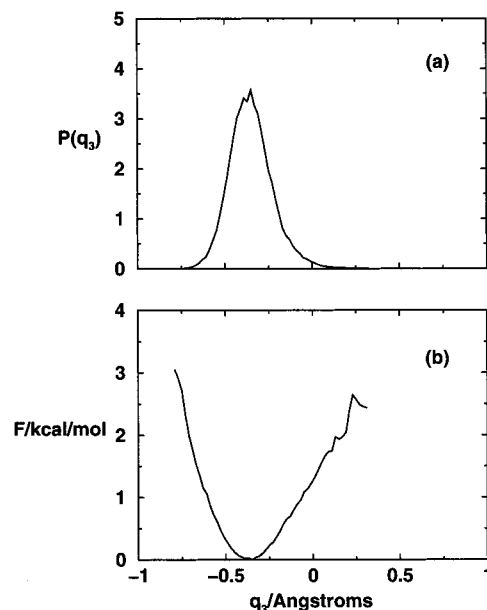


Figure 5. Calculated (a) distribution function and (b) free energy for the q_3 coordinate of crystalline NAT at 195 K from a CPMD trajectory. The q_3 coordinate contains the mobile proton H^* .

a single coordinate ensured that q_3 was a good reaction coordinate choice for proton transfer. Thus the free energy F for proton transfer was calculated from $F = -k_B \ln[P(q_3)]$, where k_B is Boltzmann's constant and T is the temperature, and presented in Figure 5b. The values of F for positive q may not be completely reliable, since many more rare proton transfer events would have to be sampled to completely converge the distribution function. However, $F|_{q=0}$ has been estimated at 1.3 ± 0.2 kcal/mol ($3.3 k_B T$), giving an idea of the energy required for the proton to classically reach the center of the OO pair.

B. Vibrational Properties. The vibrations of crystalline NAT at 195 K were analyzed from the CPMD trajectory. The Fourier transform (FT) of the calculated velocity autocorrelation function yields the power spectrum, which gives information on the vibrational frequencies of crystalline NAT. To unambiguously determine the molecular motions associated with a particular vibrational frequency, different atomic components of the power spectra were calculated along with the FT of autocorrelation functions which isolate specific molecular motions (i.e., torsional motion, etc.). The power spectra are shown for all atoms as well as individual atoms from NO_3^- , H_2O , and H_3O^+ in Figures 6a–d, respectively. In addition, the spectrum due to H^* alone is shown in 6e along with the FT of the autocorrelation function for the asymmetric stretch coordinate ν_3 of H_3O^+ . Table 3 presents assignments of vibrational frequencies obtained from our simulation and from earlier experiments of Ritzhaupt and Devlin¹¹ as well as recent experiments of Tso and Leu.¹⁶ Other experimental data exists^{12–15} and is consistent with the aforementioned experiments.

The high-frequency peaks corresponding to asymmetric $\nu_3 = 3097$ cm^{-1} and symmetric $\nu_1 = 2997$ cm^{-1} stretches of H_2O are red shifted ~ 300 cm^{-1} ($\sim 10\%$) compared to experiment. This red shifting has been observed in several applications^{32,37} and has been attributed the use of pseudopotentials³⁷ and the GGAs used to treat exchange and correlation.³⁸ This red shifting of high-frequency modes is well-known and is due to the error incurred by the use of DFT pseudopotentials.^{32,38} Nevertheless, assignment of the spectral peak positions is a useful complement to experiment. The next lower frequency peaks correspond to the H_3O^+ symmetric $\nu_1 = 2720$ cm^{-1} and asymmetric $\nu_3 =$

TABLE 3: Assignment of Vibrational Frequencies for Crystalline NAT Obtained from CPMD Simulation at 195 K and Experimental Measurements^a

species	motion ^f	simulation (ν/cm^{-1})	simulation (ν/cm^{-1} ranges)	experiment ^a (ν/cm^{-1})	experiment ^b (ν/cm^{-1})
H ₂ O	ν_3 a-stretch	3097	3180–3030	3424	3370
H ₂ O	ν_1 s-stretch	2997	3060–2905	3203	3220
H ₃ O ⁺	ν_1 s-stretch	2720	2770–2614	2920 ^c	2410
H ₃ O ⁺	ν_3 a-stretch	2497, 2000	2645–2394, 2133–1866	2920 ^c	2750
H ₃ O ⁺	ν_4 a-bend	1595, 1531	1646–1550, 1560–1504	1753	1825
H ₂ O	ν_2 bend	1538	1606–1496	1652	1665
NO ₃ ⁻	ν_3 a-stretch	1268	1292–1228	1393	1380, 1335
NO ₃ ⁻	ν_1 s-stretch	1196	1236–1174	<i>d</i>	1195
H ₃ O ⁺	ν_2 umbrella	1232	1260–1181	1110	
NO ₃ ⁻	ν_4 a-bend	732, 668	764–670, 677–630		821, 735, 710 ^e
NO ₃ ⁻	ν_2 umbrella	716	756–646		821, 735, 710 ^e
all	torsion		530–996		
unassigned	unassigned		530–996	430–820	602

^a Reference 11 at 50 K. ^b Reference 16 at 173–198 K. ^c Described as a very broad band. ^d Absent 50 K spectra, but observed in 175 K ~ 1200 cm^{-1} . ^e No distinction made between asymmetric or symmetric bending. ^f a: asymmetric. s: symmetric.

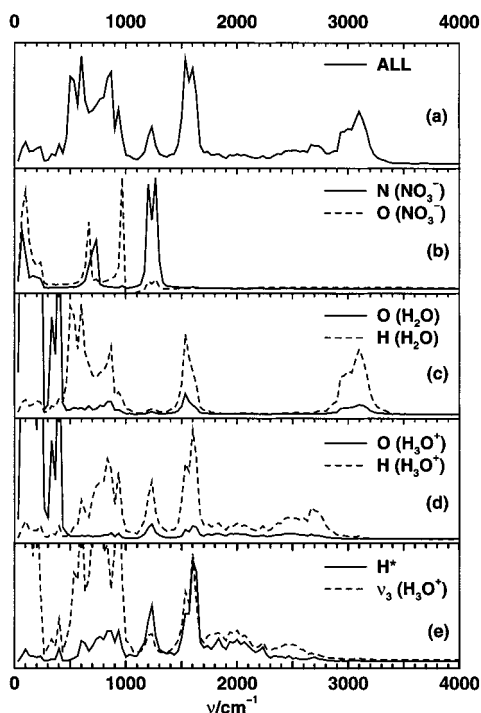


Figure 6. Calculated spectra of crystalline NAT at 195K from a CPMD trajectory. Power spectra from (a) all atoms, (b) atoms from NO₃⁻, (c) atoms from H₂O, (d) atoms from H₃O⁺, and (e) power spectrum from H* and Fourier transformed asymmetric stretch ν_3 autocorrelation function for H₃O⁺.

2497, 2000 cm^{-1} stretches. Although the agreement to recent experimental stretching frequencies¹⁶ improves, the individual peak assignments differ for asymmetric and symmetric stretches. Evident in the calculated spectra from the ν_3 autocorrelation function (Figure 6e), the ν_3 peak is clearly at lower frequencies within the stretching bands. The spectra for H*, also presented in Figure 6e, shows the splitting of the ν_3 band is completely due to the hyperextension of the O–H* bond that occurs on a longer time scale.

Modes associated with bending motions in H₃O⁺ occur at frequencies $\nu_4 = 1595, 1531 \text{ cm}^{-1}$ (asymmetric) and $\nu_2 = 1232 \text{ cm}^{-1}$ (symmetric umbrella). The H₂O bend frequency occurs at $\nu_2 = 1538 \text{ cm}^{-1}$. The symmetric ν_2 bending frequencies are easily distinguished from comparison of atomic contributions from Figures 6c and d. The H₃O⁺ umbrella mode was identified from the spectra of dipole autocorrelation function, which

showed a sharp enhancement for the ν_2 frequency. The umbrella mode is only assigned in the older experiment.¹¹

Calculations give NO₃⁻ stretches $\nu_3 = 1268 \text{ cm}^{-1}$ (asymmetric) and $\nu_1 = 1196 \text{ cm}^{-1}$ (symmetric), which are shown in Figure 6b. Since the spectra were particularly complicated at these lower frequencies, the frequencies from separate ν_3 and ν_1 autocorrelation functions were calculated to eliminate ambiguities. The ν_3 peak appeared as a singlet, in disagreement with recent experiments¹⁶ and in agreement with older experiments.¹¹ In the older experiments,¹¹ spectra were measured at both 50 and 175 K. At the lower temperature, the ν_1 peak is absent due to the reduced thermal motions of the crystal, which causes increased symmetry of NO₃⁻, rendering ν_1 dipole inactive at very low temperatures. However, at 175 K, the peak is indeed present at ~1200 cm^{-1} .

The NO₃⁻ bending modes occur at $\nu_4 = 732, 668 \text{ cm}^{-1}$ (asymmetric) and $\nu_2 = 716 \text{ cm}^{-1}$ (umbrella). The peaks were identified from the spectra of ν_3 and ν_1 autocorrelation functions. Recent experiments¹⁶ do not distinguish between types of bending motions, and the older experiment¹¹ does not assign the vibrations that exist within the NO₃⁻ frequency range.

At lower frequencies between 530 and 965 cm^{-1} , vibrations occur due to hindered rotations or librations,³⁹ which is also reflected in spectra from torsional autocorrelation functions. Below 500 cm^{-1} , frequencies are due to lattice vibrations.

4. Conclusion

Equilibrium averages, structural, and vibrational properties have been calculated for crystalline NAT at 195 K using CPMD trajectories. The simulations suggest that proton transfer occurs between unique H₃O⁺–H₂O pairs defined by the reaction coordinate q_3 . However, full proton transfer is a rare event and free energy estimates indicate that $3.3k_B T$ is required for H* to classically reach the center of the OO pair. The motion of H* is characterized as a hyperextension of the original O–H* covalent bond which is reflected by larger average bond length for O–H* and attributable to splitting of the symmetric stretch ν_3 of H₃O⁺. A comparison between simulation and experiment reflects, as expected, a 10% deviation in peak positions. Some assignments differ between experimental^{11,16} and simulation results. Discrepancies occur for the ν_1 and ν_3 stretches of H₃O, where the assignment is reversed¹⁶ and also for the peaks within 1100–1269 cm^{-1} .¹⁶ In this range, ν_3 of NO₃⁻ appears as a singlet from our calculations, while the peak is split in experiment. Also, the umbrella mode assignment from H₃O⁺ is missing from one experimental study.¹⁶ It is possible that

either the experimental assignments are incorrect or that the umbrella frequency is hidden under the large IR absorption bands in this range. Finally, the splitting of the ν_3 symmetric stretch for H_3O^+ is only seen by our simulation studies in the power spectra for H^* . Since proton transfer was only observed in the q_3 coordinate and there are seven total coordinates, the splitting may not be observable by experiment.

Recently, the gas-phase power spectra of H_9O_4^+ and H_5O_2^+ clusters have been studied by DFT,⁴⁰ where the proton was found to transfer freely between the waters of the smaller H_5O_2^+ cluster. The larger H_9O_4^+ cluster contains a stable H_3O^+ , centrally solvated by three water molecules. For the NAT crystal, the H_3O^+ is solvated by two waters and an oxygen from the neighboring NO_3^- ion. Since the proton transfer is a rare event in the crystal, the spectra is indeed more similar to the H_9O_4^+ ; both spectra have well observed contributions from the H_3O^+ ion.

CPMD results from our simulation have been used to characterize crystalline NAT at 195 K. Likely errors in the calculated $3.3k_{\text{B}}T$ proton transfer barrier are due to known limitations in DFT, which would raise the barrier, and neglected nuclear quantum effects which would lower the barrier. Although it is possible to include the effects of zero-point motions and tunneling via path integrals, the computational resources are not available at the present time for such a large system. Ideally, the IR spectra should be calculated from our simulations so that peak intensities can also be compared. This calculation involves recently developed theory and methodology⁴¹ using the Wannier function approach to compute the dipole moment. Recently, two successful applications of this method have been presented, where the IR spectra of water⁴² and ice⁴³ were calculated. Thus future studies will concentrate on computing the IR spectra and also investigating the role that NAT crystals play in enhancing the heterogeneous reaction rate, where reactions will be studied on the crystal surface.

Acknowledgment. This research was supported by generous grants from the National Institutes of Health and the National Science Foundation. The calculations were performed either on site at the Center for Molecular Modeling or at San Diego supercomputing centers using the IBM SP2 parallel machines. M.E.T. would like to acknowledge support from Grant ACS-PRF 33256-G and a grant from the Research Corporation, Grant R10218. We thank Gergely Toth for his initial correspondences regarding the simulation of NAM. We gratefully acknowledge helpful suggestions from the reviewers.

References and Notes

(1) Fahey, D. W.; Kelly, K. K.; Ferry, G. V.; Poole, L. R.; Wilson, J. C.; Murphy, D. M.; Loewenstein, M.; Chan, K. R. *J. Geophys. Res.* **1985**, *94*, 229.

- (2) Hanson, D.; Mauersberger, K. *Geophys. Res. Lett.* **1988**, *15*, 855.
 (3) Solomon, S. *Rev. Geophys.* **1988**, *26*, 131.
 (4) Tolbert, M. A.; Rossi, M. J.; Golden, D. M. *Science* **1988**, *240*, 1018.
 (5) Leu, M. T.; Moore, S. B.; Keyser, L. F. *J. Phys. Chem.* **1991**, *95*, 7763.
 (6) Taesler, I.; Delaplane, R. G.; Olovsson, I. *Acta Crystallogr.* **1975**, *B31*, 1489.
 (7) Lundgren, J.-O.; Olovsson, I. In *The Hydrogen Bond. Recent Developments in Theory and Experiments*; Schuster, P., Zundel, G., Sandorfy, C., Eds.; North-Holland: Amsterdam, 1975.
 (8) Toth, G. *J. Phys. Chem. A* **1997**, *101*, 8871.
 (9) Car, R.; Parrinello, M. *Phys. Rev. Lett.* **1985**, *55*, 2471.
 (10) Bagchi, K.; Mei, H. S.; Tuckerman, M. E.; Klein, M. L. *J. Phys. Chem. A*. Submitted for publication.
 (11) Ritzhaupt, G.; Devlin, J. P. *J. Phys. Chem.* **1991**, *95*, 90.
 (12) Smith, R. H.; Leu, M.-T.; Keyser, L. F. *J. Phys. Chem.* **1991**, *95*, 2095.
 (13) Koehler, B. G.; Middlebrook, A. M.; Tolbert, M. A. *J. Geophys. Res.* **1992**, *97*, 8065.
 (14) Toon, O. B.; Tolbert, M. A.; Koehler, B. G.; Middlebrook, A. M.; Jordan, J. *J. Geophys. Res.* **1994**, *99*, 25631.
 (15) Peil, S.; Seisel, S.; Schrems, O. *J. Mol. Struct.* **1995**, *348*, 449.
 (16) Tso, T.-L.; Leu, M.-T. *Anal. Sci.* **1996**, *12*, 615.
 (17) Hohenberg, P.; Kohn, W. *Phys. Rev. B* **1964**, *136*, 864.
 (18) Kohn, W.; Sham, L. *J. Phys. Rev. A* **1965**, *140*, 1133.
 (19) Stich, I.; Car, R.; Parrinello, M.; Baroni, S. *Phys. Rev. B* **1989**, *39*, 4997.
 (20) Galli, G.; Parrinello, M. *Phys. Rev. Lett.* **1992**, *24*, 3547.
 (21) Mauri, F.; Galli, G. *Phys. Rev. B* **1994**, *50*, 4316.
 (22) Tuckerman, M. E.; Parrinello, M. *J. Chem. Phys.* **1994**, *101*, 1302, 1316.
 (23) Martyna, G. J.; Klein, M. L.; Tuckerman, M. E. *J. Chem. Phys.* **1993**, *98*, 2796.
 (24) Martyna, G. J.; Klein, M. L. *J. Chem. Phys.* Submitted for publication.
 (25) Sprik, M. *J. Chem. Phys.* **1991**, *95*, 2283.
 (26) Blöchl, P. E.; Parrinello, M. *Phys. Rev. B* **1992**, *45*, 9413.
 (27) Peterson, S. W.; Levy, H. A. *Acta Crystallogr.* **1957**, *10*, 70.
 (28) Hutter, J.; Ballone, P.; Bernasconi, M.; Focher, P.; Fois, E.; Gödecker, S.; Parrinello, M.; Tuckerman, M. *CPMD*, Version 3.0; MPI für Festkörperforschung and IBM Research Laboratory, Stuttgart and Zürich, 1990–1996.
 (29) Kohn, W.; Becke, A. D.; Parr, R. G. *J. Phys. Chem.* **1996**, *100*, 12974.
 (30) Becke, A. D. *Phys. Rev. A* **1988**, *38*, 3098.
 (31) Lee, C.; Yang, W.; Parr, R. G. *Phys. Rev. B* **1988**, *37*, 785.
 (32) Sprik, M.; Hutter, J.; Parrinello, M. *J. Chem. Phys.* **1996**, *105*, 1142.
 (33) Tuckerman, M. E.; Marx, D.; Klein, M. L.; Parrinello, M. *Science* **1997**, *275*, 817.
 (34) Xie, Y.; Remington, R. B.; Schaefer, H. F., III, *J. Chem. Phys.* **1994**, *101*, 4878.
 (35) Troullier, N.; Martins, J. L. *Phys. Rev. B* **1991**, *43*, 1993.
 (36) Tuckerman, M. E.; Marx, D.; Klein, M. L.; Parrinello, M. *J. Chem. Phys.* **1996**, *104*, 5579.
 (37) Tuckerman, M. E.; Klein, M. L. *Chem. Phys. Lett.* **1997**, *283*, 147.
 (38) Sprik, M. Private Communication.
 (39) Hobbs, P. V. Clarendon: Oxford, 1974.
 (40) Cheng, H.-P. *J. Phys. Chem. A* **1998**, *102*, 6201.
 (41) Marzari, N.; Vanderbilt, D. *Phys. Rev. B* **1997**, *56*, 12847.
 (42) Silvestrelli, P. L.; Bernasconi, M.; Parrinello, M. *Chem. Phys. Lett.* **1997**, *277*, 478.
 (43) Bernasconi, M.; Silvestrelli, P. L.; Parrinello, M. *Phys. Rev. Lett.* **1998**, *81*, 1235.